# Multi-scale Modelling of Titanium Diboride Degradation Using Crystal Elasticity Model and Density Functional Theory

Afaf Saai[1, a], Zhaohui Wang2[1, 2, b], Micol Pezzotta[1, c], Jesper Friis[1, d], Arne Petter Ratvik[1, e], Per Erik Vullum[1, f]

[1] SINTEF Materials and Chemistry, NO-7465 Trondheim, Norway

[2] Department of Materials Science and Engineering, Norwegian University of Science and Technology, NO-7491 Trondheim, Norway

[a] afaf.saai@sintef.no (Tel. +47 93401702), [b] zhaohui.wang@sintef.no, [c] micol.pezzotta@sintef.no, [d] jesper.friis@sintef.no, [e] arne.p.ratvik@sintef.no, [f] pererik.vullum@sintef.no

## Abstract

Titanium diboride ($TiB_2$) is regarded as the most promising material to be used as inert cathodes in the electrochemical reduction of alumina to aluminium metal. $TiB_2$ is well known as a ceramic material with high strength and durability characterized by a high melting point, high hardness, and excellent mechanical and chemical wear resistances. However, one concern with this material is the variability of its properties, depending on the processing procedures and the obtained microstructure (e.g. bulk density, secondary phases, grain size). In this work, a multiscale framework is used to evaluate the degradation of the $TiB_2$ as a function of its microstructure. The mechanical and fracture parameters of $TiB_2$ and its secondary phases were determined by the density functional theory and were implemented in a crystal elasticity-finite elements model. The influence of $TiB_2$ grain size and the properties of the secondary phase on the mechanical properties and degradation mechanisms were predicted and discussed regarding the effects of material parameters identified at different scales.

**Keywords**

Inert cathode, Titanium diboride, Grains size, Secondary Phase, Multiscale modelling, Finite element, Density functional theory

## 1 Introduction

An inert cathode material must satisfy several requirements such as electronic conductivity, wettability by aluminium, low solubility, and high mechanical and thermal resistance. Titanium diboride ($TiB_2$) is a ceramic material with high melting point, high hardness, high strength, and good mechanical and chemical wear resistance. Despite having a useful combination of properties, the concern with $TiB_2$ is the variability of the properties depending on the processing procedures and the obtained microstructure. Munro [1] showed that the elastic modulus at room temperature increases with $TiB_2$ bulk density. The average grain size of $TiB_2$ was found to affect fracture toughness and flexural strength [1, 2]. Jensen et al [3] emphasised large differences in $TiB_2$ resistance towards aluminium penetration depending on the secondary phases. They observed grain boundary penetration in $TiB_2$ material containing an oxycarbide secondary phase while they could not detect Al infiltration in a material with apparently no secondary phases after 100 h.

Understanding the influence of microstructure on the mechanical and physical properties of $TiB_2$ is critical for tailoring microstructures for an industrial application such as the primary production of

aluminium. Knowing that the optimization of $TiB_2$ processing is difficult and expensive, modelling tools can save a lot of experimental efforts. A multiscale optimization procedure which combines experimental tests with numerical simulations is well suited.

In this paper, a multiscale modelling approach [4, 5] is used to investigate the influences of microstructure of $TiB_2$ on the elastic properties and degradation mechanisms. A sequential method is proposed to investigate the influence of the material parameters identified at different scales (atomic, grains and phase) on elastic and fracture properties. The representative volume element (RVE) approach [6] is used to explicitly account for $TiB_2$ microstructure in a finite element (FE) model incorporating the anisotropic elastic response of the constitute grains. The fundamental theory of the multi-scale model and the identification procedure of the model parameters are described in the first section. In the second section, the numerical results are discussed and evaluated with respect to the available experimental results.

## 2 Material and Microstructure

A $TiB_2$ specimen was examined by scanning electron microscope (SEM) and transmission electron microscopy (TEM) to define microstructural characteristics of $TiB_2$ and the properties of the secondary phases. The backscattered electron image in Fig. 1 shows the size and the morphology of the $TiB_2$ grains. The secondary phases show up as small, bright contrast grains in this image. From X-ray diffraction (XRD) a preferred orientation of the $TiB_2$ grains along the [0001] direction was observed. Furthermore, electron backscatter diffraction (EBSD) was used to map the crystalline grain orientations, and the distribution of mis-orientations between grains is shown in Fig. 2. More than 75 % of all grain boundaries are qualified as high-angle grain boundaries with a mis-orientation larger than 15°.

The SEM micrograph (Fig. 1) further shows that the secondary phase (white spots) is mainly located at the grain boundaries. The surface fraction of the secondary phase ($f_P = 1.014\ \%$) was determined by an in-house code based on processing of SEM images. The composition of the secondary phase was defined by high angle annular dark field scanning TEM (HAADF STEM) (Fig. 3). Spectrum imaging by electron energy loss spectroscopy (EELS) and X-ray energy dispersive spectroscopy (EDS) showed that the secondary phase consisted of Ti, N and C. Further quantifications of the spectroscopy data indicated that the secondary phase is $Ti_2NC$. An electron diffraction pattern from a region covering both $TiB_2$ and the secondary phase is shown in Fig. 3a. $TiB_2$ reflections are indexed by red Miller-Bravais indices, while the face centred cubic (fcc) secondary phase is indexed by white Miller indices. The high-resolution STEM image in Fig. 3b shows the orientational relationship between the $TiB_2$ and the secondary phase. At the imaged interface, the [0001] and [10-10] directions of $TiB_2$ are parallel to the [111] and [11-2] directions of the secondary phase. At the grain boundary interface, the (0001) plane of $TiB_2$ faces the (111) plane of the secondary phase.

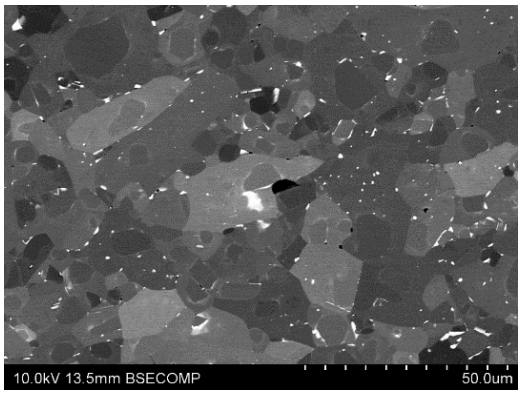

Fig. 1 SEM image of $TiB_2$ microstructure showing the distribution of the secondary phase

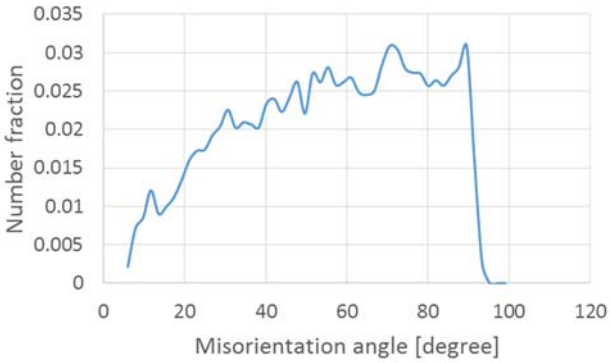


Fig. 2 Mis-orientation angles measured by EBSD for $TiB_2$ grains

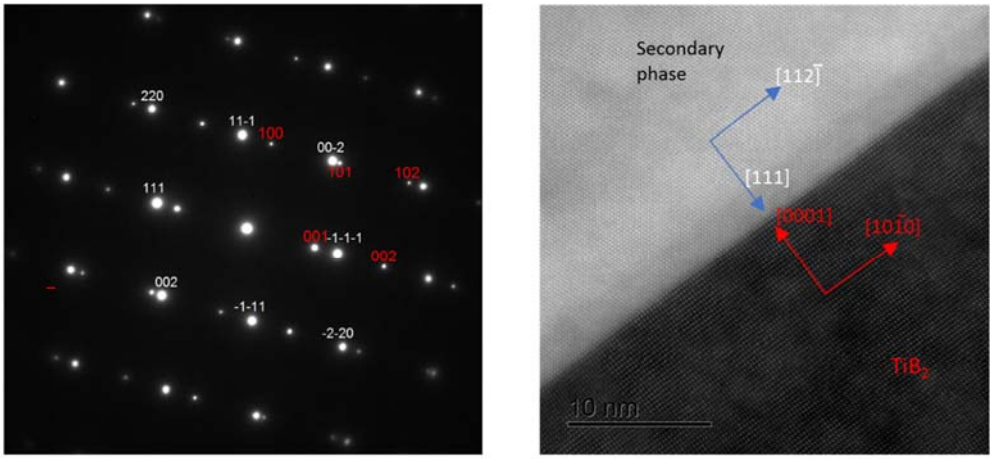


Fig. 3 (a) Electron diffraction pattern from a region covering both the $TiB_2$ and the secondary phase. In (b) a high resolution HAADF STEM image from the interface between the $TiB_2$ and the $Ti_2CN$ secondary phase are shown

Experimental observations related to diffusion mechanisms in $TiB_2$ reported a high fraction of oxygen (0.8 wt%) in specimens exposed to sodium. The oxygen content was expected to be related to a secondary titanium monoxide (TiO) phase, which also has a FCC crystal structure. It is hard to detect such secondary phases by microscopy analysis. The multiscale model however, is well suited to investigate the influence of such secondary phase.

From this analysis, two sets of simulations were defined. The first investigates the influence of $TiB_2$ grains, and the second investigates the influence of secondary phases properties. We restrict these simulations to dense material to exclude the influence of density. Ledbetter and Tanaka [7] estimated the values of elastic modulus for full dense polycrystalline $TiB_2$ from the elastic constants of $TiB_2$ single crystal measured by resonance ultrasound spectroscopy. The value of E=584.7 GPa obtained by Ledbetter and Tanaka was higher than the value reported by Spoor et al. [8] (E=579 GPa) and the value defined by Munro [1] for dense $TiB_2$ material (E=565 GPa). The increasing mass fraction of $TiB_2$ in the specimen was found to increase the elastic modulus as reported by Munro [1] and Bucher et al [2].

# 3 Multiscale modelling

The multiscale modelling approach used here involves the finite elements model, crystal elasticity (CE) model, and the density functional theory (DFT). Different RVEs representing different average grain

size and different properties of the secondary phase (treated here as grains with different orientations) were generated and implemented in a FE model incorporating the anisotropic elastic response of the constitute grains. The elastic constants of $TiB_2$ grains and the secondary phase grains were identified by DFT. Brittle fracture is assumed in $TiB_2$ grains and in the secondary phase. An energy-based failure criterion using the work of separation for the material interfaces has been identified using DFT [4, 9]. This criterion was implemented in the finite element model to determine tensile strength of the RVE.

## 3.1 Finite Element Model

Fig. 4 illustrates the finite element model of $TiB_2$ RVE and the periodic boundary conditions representing tensile load. The FE model consists of a periodic RVE with 800 grains discretized by FE method to account for the gradient of deformation in the grains. Each grain in the RVE was divided into two sub-sets: the first contains the elements on the grain boundary, called "grain interface set", while the second excludes the grain boundary elements from the grain set, called "inside grain set". The grain interface set and the inside grain set have the same elastic properties and different fracture properties. The secondary phase is represented by a set of elements randomly distributed on the grain interfaces. Each element in the secondary phase set represents a grain randomly oriented. Tensile load is applied on the RVE with respect to the periodicity conditions as illustrated in Fig. 4. The RVE has four master nodes, which are referred to by full black circles. The master node 0 is fixed, the master node 1 is subjected to a constant velocity in the tensile direction (x) and the master node 2 and 3 are free to move in y direction and z direction respectively. The displacements of the nodes 1, 2 and 3 are zeroed in Y direction, Z direction and X direction respectively.

Periodic boundary conditions are applied to the nodes located on the faces of the RVE to ensure periodicity in displacements and minimize constraint effects. The periodicity equations read:

$$v_i^a - v_i^b = v_i^R - v_i^0 \qquad i = x, y, z \tag{1}$$

where *a* is a node located on a reference side of the RVE, *b* is a node located on the opposite side, $v_i^a$ and $v_i^b$ are the velocities of nodes $a$ and $b$, respectively, $v_i^R$ is the velocity of the reference node (1, 2 or 3) located on the same side as b, and $v_i^0$ is the velocity of the master node 0.

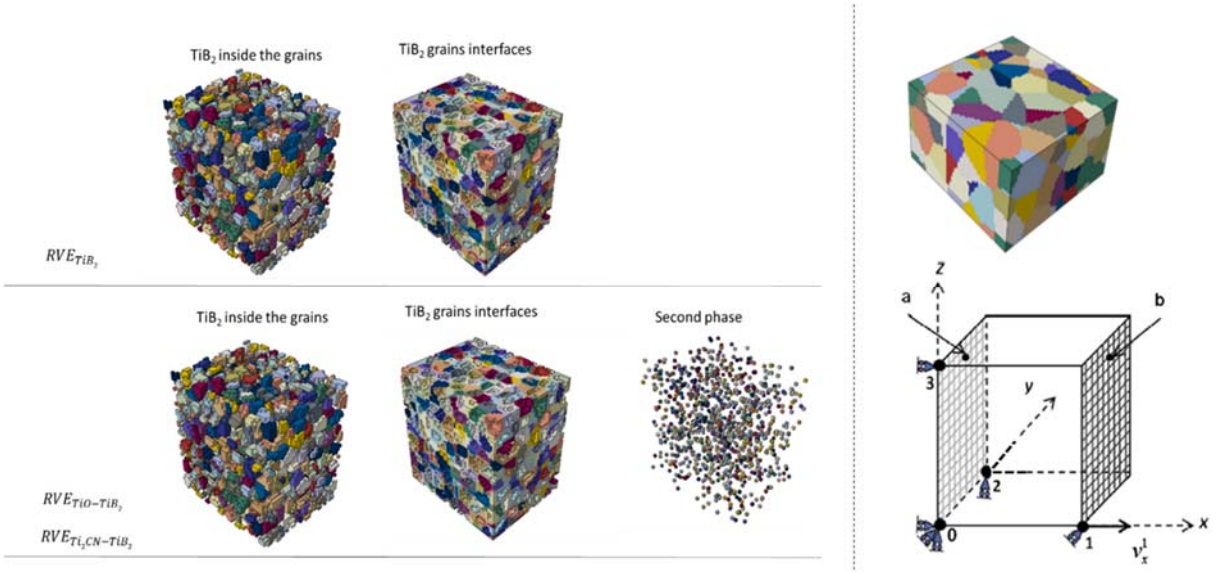


Fig. 4 Representative volume element of $TiB_2$ microstructure used in the FE simulations

## 3.2 Material models

The response of $TiB_2$ grains and the response of the secondary phase are assumed to be elastic with linear stress-strain relationship. The overall, or average, tensile stress state of the RVE is obtained by a volume average of all stresses over all individual grains within the RVE:

$$\langle \boldsymbol{\sigma} \rangle = \sum_{g=1}^{n_g^T} f_g^T \boldsymbol{\sigma}_g^T + \sum_{g=1}^{n_g^P} f_g^P \boldsymbol{\sigma}_g^P \tag{2}$$

The superscript $T$ refers to $TiB_2$ grains and $P$ refers to the secondary phase, $f_g$ is the volume fractions of a grain $g$, $n_g$ is the number of grains, and $\boldsymbol{\sigma}_g$ is the Cauchy stress tensor. Cauchy stress tensor for the individual grains is given:

$$\boldsymbol{\sigma}_g = \sum_{e=1}^{n_e^g} \left( \sum_{ip=1}^{n_{ip}} f_{ip}^g \boldsymbol{\sigma}_{ip} \right)_e \tag{3}$$

$\boldsymbol{\sigma}_{ip}$ is Cauchy stress for the integration points $ip$, $f_{ip}^g = V_{ip}/V_g$ are the volume fractions of integration point $ip$ in grain $g$, $n_{ip}$ is the number of integration point in the element $e$, and $n_e^g$ are the numbers of elements in the grain $g$.

The Cauchy stress for each integration point is computed using hyper-elasticity model with polar decomposition of the gradient of deformation: $F^e = R \cdot U$ , where $R$ is the initial crystallographic orientation of the grain and $U$ is the right elastic stretch tensor. The elastic deformation of each grain is described in the local reference of the grain by the generated Hooke's law which accounts for the three-dimensional anisotropic linear response to the applied stresses:

$$\sigma_I = C_{IJ}\varepsilon_J \qquad (I,J = 1,2,3,\dots,6) \tag{4}$$

$\sigma_I$ and $\varepsilon_I$ are the independent components of stress and strain and $C_{IJ}$ is the stiffness tensor. For the hexagonal crystal system, five independent components (elastic constants) are needed to describe the stiffness tensor:

$$\boldsymbol{C} = \begin{bmatrix} C_{11} & C_{12} & C_{13} & 0 & 0 & 0 \\ C_{12} & C_{11} & C_{13} & 0 & 0 & 0 \\ C_{13} & C_{13} & C_{33} & 0 & 0 & 0 \\ 0 & 0 & 0 & C_{44} & 0 & 0 \\ 0 & 0 & 0 & 0 & C_{44} & 0 \\ 0 & 0 & 0 & 0 & 0 & \dfrac{C_{11}-C_{12}}{2} \end{bmatrix} \tag{5}$$

For the FCC crystal system, three independent components are needed:

$$\boldsymbol{C} = \begin{bmatrix} C_{11} & C_{12} & C_{12} & 0 & 0 & 0 \\ C_{12} & C_{11} & C_{12} & 0 & 0 & 0 \\ C_{12} & C_{12} & C_{11} & 0 & 0 & 0 \\ 0 & 0 & 0 & C_{44} & 0 & 0 \\ 0 & 0 & 0 & 0 & C_{44} & 0 \\ 0 & 0 & 0 & 0 & 0 & C_{44} \end{bmatrix} \tag{6}$$

A fracture model derived from Griffith-like criterion for brittle materials [4, 9] is utilized in the FE simulations to predict fracture initiation in the RVE. It assumes that fracture is initiated in an element when the supplied stored energy of the element exceeds a critical threshold:

$$\left(\frac{1}{2}\sum_{j,j}\sigma_{ij}\varepsilon_{ij}^{e}\right)A \geq 2\,W_{sep}\Delta L \tag{1}$$

The left-hand side is the elastic energy per unit length in which $\sigma_{ij}$ and $\varepsilon_{ij}^{e}$ are the components of stress and strain tensors, respectively, and $A$ is the element area. The right-hand side is the critical threshold representing the energy needed to separate a material interface into two free surfaces, where $W_{sep}$ is the work of separation [J/m$^2$], and $\Delta L$ is the length of the element edge.

# 4 Identification of material parameters

The values of single crystal elastic constants (SCEC) for $TiB_2$ and secondary phases, and the work of separation $W_{sep}$ are determined by DFT computation constructed using microscopic observations of material microstructure (Section 2). The DFT calculations were performed using the Vienna Ab initio simulation package (VASP) [10, 11]. The exchange-correlation contribution to the total energy was approximated within the generalized gradient approximation (GGA) formalism using the Predew-Burke-Ernzerhof (PBE) functional [12]. The energy cutoff was set to 415 eV, and the ion-electron was described using the projector-augmented wave (PAW) method [13]. The Brillouin zone was sampled by $2 \times 6 \times 1\Gamma$ centred grid for $TiB_2$ grain boundaries and similar k-points density for the other geometries.

The microscopic observations in Section 2 were used to construct the interface models and to select the face direction of the interfaces. Three material interfaces were considered: $TiB_2$-$TiB_2$ grain interfaces, $TiB_2$-TiO interface and $TiB_2$-$Ti_2CN$ interface (see Fig. 5). For the $TiB_2$-$TiB_2$ grain boundary, two twin boundaries were constructed with 27.8° and 81.8° mis-orientation, respectively. The $TiB_2$-TiO interface was constructed such that the misfit between different materials systems was minimised, while the $TiB_2$-$Ti_2CN$ interface was constructed directly from the experimental observations in Fig. 3. All atoms in the supercell could relax during structural optimization.

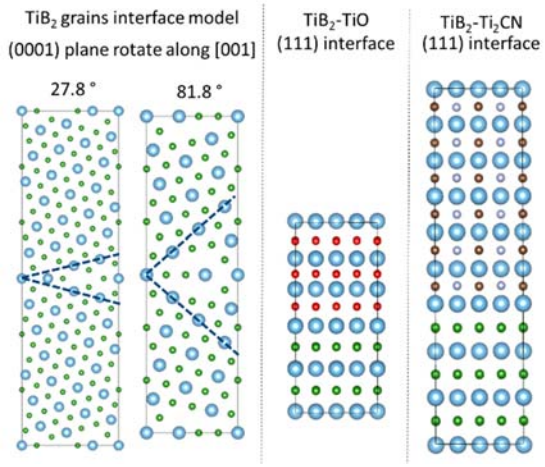


Fig. 5 The interface models for $TiB_2$-$TiB_2$ grain interfaces (with low and high boundary angles), $TiB_2$-TiO interface and $TiB_2$-$Ti_2CN$ interface

SCEC determined by DFT are given in

. The values of SCEC obtained in the present work have higher value of $C_{44}$ compared to value obtained by Milman and Warren [14] ($C_{11} = 656\ GPa,\ C_{12} = 66\ GPa,\ C_{13} = 98\ GPa,\ C_{33} = 461GPa,$ and $C_{44} = 259\ GPa$). The SCEC measured by Ledbetter and Tanaka [7] ($C_{11} = 645.4\ GPa,\ C_{12} = 48.98\ GPa, C_{13} = 95.25\ GPa, C_{33} = 458.1GPa,$ and $C_{44} = 262.6\ GPa$) have lower values of SCEC, in particularly $C_{12}$, compared to both DFT in the present work and Milman and Warren [14].

Table 1 Single crystal elastic constants in [GPa] for $TiB_2$, $Ti_2CN$ and TiO

| | $C_{11}$ | $C_{12}$ | $C_{13}$ | $C_{33}$ | $C_{44}$ |
|---|---|---|---|---|---|
| $TiB_2$ | 656.9 | 65.8 | 102.5 | 453.4 | 261.2 |
| $Ti_2CN$ | 577.5 | 111.9 | 111.9 | 577.5 | 194.0 |
| TiO | 598.2 | 93.5 | 93.5 | 598.2 | 27.9 |

**Error! Reference source not found.** gives the values of $W_{sep}$ determined by the DFT in the present work. As can be observed, the initiation of microcrack inside the grain requires more energy compared to the grain boundary. The low angle grain boundary has slightly lower $W_{sep}$ than the high angle grain boundary. The $W_{sep}$ for high angle grain boundary will be implemented in the FE simulations since the mis-orientations in Fig. 2 are dominated by high-angle grain boundaries. The $TiB_2$-TiO interface has higher $W_{sep}$ than the $TiB_2$-$Ti_2CN$ interface.

Table 2 The work of separation $W_{sep}$ $[J/m^2]$ obtained by DFT for the microstructure interfaces

| $TiB_2$-TiO | $TiB_2$-$Ti_2CN$ | $TiB_2$ high-angle grain boundary | $TiB_2$ low-angle grain boundary | inside $TiB_2$ grains |
|---|---|---|---|---|
| 8.03 | 7.40 | 6.26 | 6.20 | 8.75 |

# 5 Results

## 5.1 Influence of average grain size

Four RVEs representing 4 virtual $TiB_2$ specimens with different average grain sizes ($d_{TiB2}$= 2, 7, 10, and 15 µm) were generated. Each RVE consists of 800 grains having random orientations. The same set of random orientations was used in all RVEs. The size of the different RVEs were adjusted to obtain the same number of grains with respect to the associated grain size. The boundary conditions described in Fig. 4 were applied to all RVEs.

Two series of CE-FE simulations were performed to evaluate the effect of the SCEC on elastic modulus and tensile strength. The first serial implements the SCEC identified in the present work, while the second serial implements the SCEC by Milman and Warren [14]. The elastic modulus ($E$) and tensile strength ($\sigma_T$) for the different RVEs were extracted. As expected, the grain size of $TiB_2$ has negligible effect on $E$. The elastic modulus obtained by CE-FE simulations with the SCEC of the present work is $619 \pm 1.4$ GPa, where the standard deviation ($\pm 1.4$) represents the effect of the grain size. The elastic modulus obtained by CE-FEM with the SCEC of Milman and Warren was $595.6 \pm 1.4\ GPa$. The difference between the two values of $E$ represent the sensitivity of $E$ to the SCEC. Ledbetter et Tanaka [7] found lower value of $E$ ( $584.7\ GPa$) determined from SCEC using a Voigt-Reuss-Hill approach [15]. It should be noticed here that Ledbetter and Tanaka has lower values of SCEC compared to SCEC obtained by DFT computations (see Section 4).

Tensile strength for the different RVEs is given in

. As can be observed, FE simulations with DFT identification of $W_{sep}$ overestimate the tensile strength compared to tensile strength typically used for $TiB_2$. This can be explained by the fact that DFT calculations are performed on idealised atomistic models without microstructural defects, while such defects are highly present in reality and reduces the energy required for fracture initiation. CE-FE simulations however predict the increase of $\sigma_T$ with the decrease of average grain size. A similar influence of the grain size on flexural fracture was reported in the review of Munro [1].

Table 3 Tensile strength by CE-FE simulations with the DFT identification of $W_{sep}$

| $d_{TiB2}$ (µm) | 2.0 | 7.0 | 10.0 | 15.0 |
|---|---|---|---|---|
| $\sigma_T$[MPa] | 3381 | 1930 | 1617 | 1305 |

The CE-FE simulations predict the initiation of the microcrack in the elements on $TiB_2$ grain boundary. This can be explained by the energy based criterion (Equation (1)). As illustrated in Fig. 6, heterogeneous distribution of the elastic energy densities (left-hand side of Equation (1)) is obtained by CE-FE simulations due to the gradient of deformation related to the differences between neighbouring grain orientations. The element on $TiB_2$ grains interface emit higher energy density than the elements inside the grains. In the case of the RVE with $2\mu m$ grain size, the energy required to initiate microcrack in an element inside the grain (right hand side of Equation (1)) is $3.5 \times 10^{-3}\, J/m$, while the energy density requested to initiate microcrack in an element on the grain boundary is $2.5 \times 10^{-3}\, J/m$. As can be observed in Fig. 6, the fracture criterion is shown in the most deformed elements on the grain boundary.

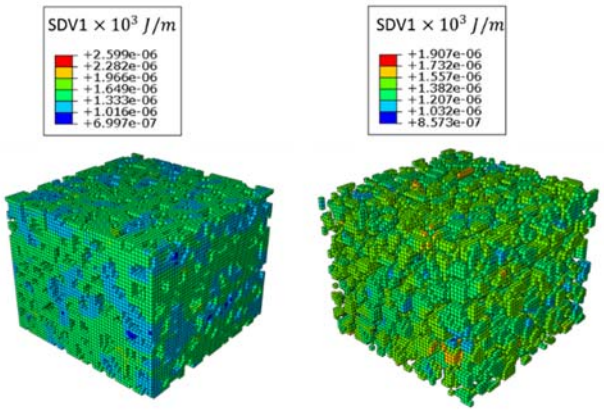


Fig. 6 Distribution of elastic energy densities inside the grains (right) and on the grain interfaces (left)

## 5.2 Influence of the properties of the secondary phases

CE-FE simulations were performed on three RVEs. The first RVE contains 800 $TiB_2$ grains with average grain size of 2 µm. The second RVE contains 800 $TiB_2$ grains with average grain size of 2 µm and 1 % of secondary phase $Ti_2CN$, randomly distributed on $TiB_2$ grain boundaries. The third contains 800 $TiB_2$ grains with an average grain size of 2 µm and 1 % of the secondary phase TiO randomly distributed on $TiB_2$ grain boundaries. Random orientations are associated to the $TiB_2$, $Ti_2CN$ and TiO grains. The same set of random orientations were used in all RVEs. The SCEC and $W_{sep}$ identified by DFT for $TiB_2$, $Ti_2CN$ and TiO have been implemented.

The elastic modulus and tensile strength were extracted for all RVEs and represented in **Error! Reference source not found.**. As can be observed, both secondary phases reduce the elastic modulus and tensile strength. This is consistent with the experimental observation in the review of Munro [1].

However, the reduction of the elastic modulus is found to be dependent on the properties of the secondary phases. The lowest elastic modulus is associated to $TiB_2$-TiO RVE. CE-FEM with DFT identification of $W_{sep}$ overestimates the tensile strength for the different RVEs. As explained above, this results from the assumption of perfect interface in the DFT calculations.

Table 4 The elastic modulus (E) and tensile strength ($\sigma_T$) predicted by CE-FE simulations

| RVE | $TiB_2$ | $TiB_2$-TiO | $TiB_2$-$Ti_2CN$ |
|---|---|---|---|
| E (GPa) | 619 | 612.2 | 614.3 |
| $\sigma_T$ (MPa) | 3381 | 2750 | 3300 |

The distribution of the elastic energy densities (left-hand side of Equation (7)) in the $TiB_2$-TiO RVE is given in Fig. 7 at the moment of microcrack initiation. The energy density required to initiate a microcrack inside a $TiB_2$ grain (right hand side of Equation (1)) is $3.5 \times 10^{-3}\ J/m$, while the energy densities required for crack initiation in $TiB_2$ grain boundary and $TiB_2$-TiO interface are respectively $2.5 \times 10^{-3}\ J/m$ and $3.3 \times 10^{-3}\ J/m$. CE-FEM predicts the initiation of the microcrack in elements on $TiB_2$ grain boundary close to TiO. The TiO increases the gradient of deformation in the elements on the grain boundary where highest energy density is observed. The fracture is initiated in $TiB_2$-TiO RVE at lower tensile stress than $TiB_2$-$Ti_2CN$ RVE (**Error! Reference source not found.**). This is explained by the difference between the material properties of TiO and the material properties of $Ti_2CN$ (see

and **Error! Reference source not found.**).

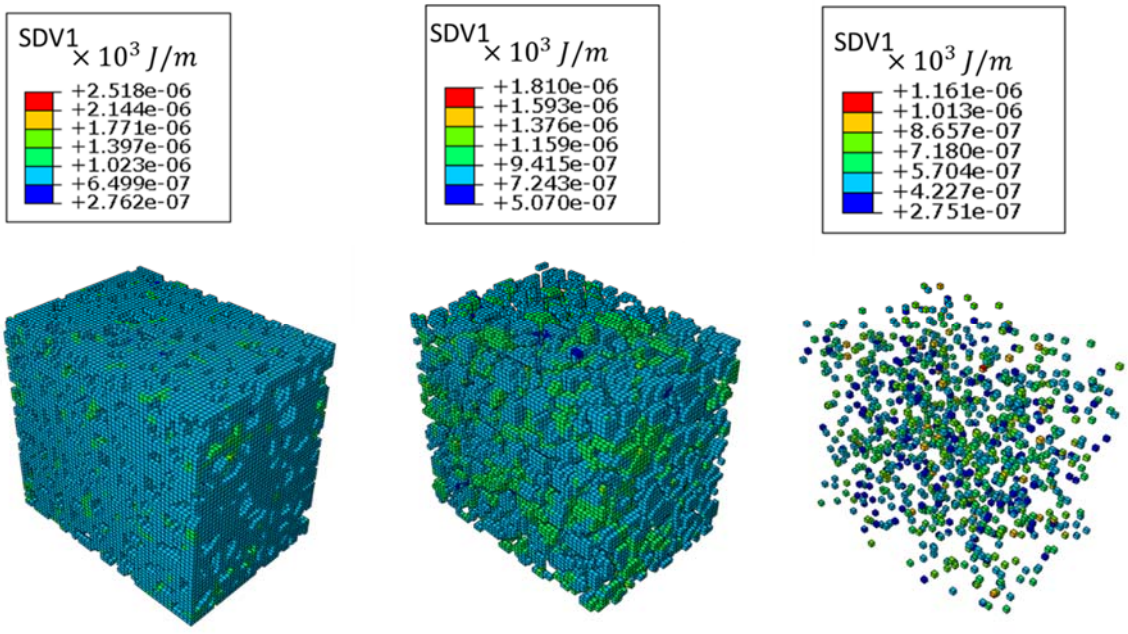


Fig. 7 Distribution of elastic energy densities on the $TiB_2$ grain interfaces (left), inside $TiB_2$ grains (middle) and in the secondary phase TiO (right)

## 6 Discussion and Conclusion

A sequential method was used to investigate the influences of material parameters identified at different scales (atomic, grain and phase) on elastic and fracture properties of titanium diboride. FE simulations incorporating CE model were performed on different RVEs of $TiB_2$ material. Single crystal elastic constants and fracture parameters were identified by DFT computations.

The DFT calculations in the present work predicted higher values of SCEC than the values measured by Ledbetter and Tanaka (2009). This increased the value of elastic modulus compared to the value estimated by Ledbetter and Tanaka. The fracture parameters identified by DFT overestimated the fracture strength. The work of separation is determined by DFT assuming perfect interface while the real material includes microstructural defects that reduce the energy necessary for initiation and propagation of microcrack. These defects should be considered in the calibration procedure of the work of separation.

CE-FE simulations of $TiB_2$ RVE with 1 % of secondary phase TiO indicate a reduction in the elastic modulus and tensile strength compared to full dense $TiB_2$ material. The elastic modulus and fracture strength predicated by CE-FE simulations depend on the properties of the secondary phase. Elastic modulus and tensile strength for $TiB_2$-TiO RVE are lower than elastic modulus and tensile strength for $TiB_2$-$Ti_2CN$ RVE. The microcracks in the CE-FE simulations are initiated in the elements on the $TiB_2$ grain interface due to the gradient of deformation. The secondary phase TiO increased the gradient of deformation in the elements on the grain boundary due to the difference between $TiB_2$ properties and TiO secondary phase properties.

Based on CE-FE simulations, $TiB_2$ material with refined grain size is recommended for increased fracture strength. It is also suggested to consider the properties of the secondary phase during the assessment of mechanical properties of $TiB_2$. With enhanced identification of fracture parameters, the CE-FE simulations can be recommended as an optimization tool to define the tolerance range of microstructure features such as fraction and properties of secondary phase, grain size, crystallographic texture and $TiB_2$ bulk density.

## Acknowledgement

The financial support of this work from Norsk Hydros Fond for SINTEF is gratefully acknowledged. Computational resources were provided by Sigma2 (The Norwegian Metacenter for High Performance Computing) through Project NN9264K and ntnu243. Thanks to Wilhelm Dall for helping with EBSD analysis.

## References

[1] Munro RG (2000) Material Properties of Titanium Diboride. Journal of Research of NIST 105(5): 709–720

[2] Becher PF, Finch CB, and Ferber MK (1986) Effect of Residual Nickel Content on the Grain Size Dependent Mechanical Properties of TiB2. J. Mat. Sci. Lett. 5: 195-197

[3] Jensen MS, Pezzotta M, Zhang ZL, Einarsrud M-A, Grande T. (2008) Degradation of $TiB_2$ ceramics in liquid aluminum, J. Eur. Ceram. Soc. 28: 3155–3164

[4] Saai A, Svenum I-H, Kane PA, Friis J, Berstad T (2014) Multi-scale modeling of WC-Co drill bits material with density functional theory and crystal elasticity model, Procedia Mater. Sci. 3: 640 – 645

[5] Saai A, Hopperstad OS, Granbom Y, Lademo O-G (2014) Influence of volume fraction and distribution of martensite phase on the strain localization in dual phase steels, Procedia Mater. Sci. 3: 900 – 905

[6] Prakash A, Weygand SM, Riedel H (2009) Modeling the evolution of texture and grain shape in Mg alloy AZ31 using the crystal plasticity finite element method. Comput. Mater. Sci 45: 744–750

[7] Ledbetter H and Tanaka T (2009) Elastic-Stiffness Coefficients of Titanium Diboride. J Res Natl Inst Stand Technol. 114(6): 333–339

[8] Spoor PS, Maynard JD, Pan MJ, Green DJ, Hellmann JR, and Tanaka T (1997) Elastic Constants and Crystal Anisotropy of Titanium Diboride, Appl. Phys. Lett. 70: 1959-1961
[9] Kim CS, Massa TR, Rohrer, GS (2006) Modeling of the relationship between microstructural features and the strength of WC–Co composites. Int. J. Refract. Metals Hard Mater. 24: 89–100
[10] Kresse G and Hafner J (1993) Ab. initio molecular dynamics for liquid metals. Phys. Rev. B 47: 558–561
[11] Kresse, G and Hafner J (1993) Ab initio molecular dynamics for open-shell transition metals Phys. Rev. B 48: 13114–13188
[12] Perdew JP, Burke K, Ernzerhof M (1996) Generalized Gradient Approximation Made Simple. Phys. Rev. Lett. 77: 3865–3877
[13] Bloch PE (1994) Projector augmented-wave method. Phys. Rev. B 50: 17953–17979.
[14] Milman V and Warren MC (2001) Elastic properties of $TiB_2$ and $MgB_2$. J. Phys.: Condens. Matter 13: 5585–5595
[15] Ledbetter H. (2000) Monocrystal-polycrystal elastic-constant models, in Handbook of Elastic Properties of Solids, Liquids, and Gases. III. Academic; New York: 313–324